

# Diffuse emission measurement with *INTEGRAL/SPI* as indirect probe of cosmic-ray electrons and positrons

Laurent Bouchet<sup>1,2</sup>, Andrew W. Strong<sup>3</sup>, Troy A. Porter<sup>4</sup>, Igor V. Moskalenko<sup>4</sup>, Elisabeth Jourdain<sup>1,2</sup>, and Jean-Pierre Roques<sup>1,2</sup>

bouchet@cesr.fr

## ABSTRACT

Significant advances have been made in the understanding of the diffuse Galactic hard X-ray continuum emission using data from the *INTEGRAL* observatory. The diffuse hard power-law component seen with the *INTEGRAL/SPI* spectrometer has been identified with inverse-Compton emission from relativistic (GeV) electrons on the cosmic microwave background and Galactic interstellar radiation field. In the present analysis, SPI data from 2003 to 2009, with a total exposure time of  $\sim 10^8$  s, are used to derive the Galactic ridge hard X-ray spatial distribution and spectrum between 20 keV and 2.4 MeV. Both are consistent with predictions from the GALPROP code. The good agreement between measured and predicted emission from keV to GeV energies suggests that the correct production mechanisms have been identified. We discuss the potential of the SPI data to provide an indirect probe of the interstellar cosmic-ray electron distribution, in particular for energies below a few GeV.

*Subject headings:* Galaxy: general — Galaxy: structure — gamma rays: observations

## 1. Introduction

The Galactic ridge is known to be an intense source of continuum hard X-ray and  $\gamma$ -ray emission. The hard X-ray emission was discovered by a rocket experiment in 1972 (Bleach et al. 1972), and interstellar emission has subsequently been observed from keV to MeV energies by the satellites HEAO-1, EXOSAT, Temna, ASCA, Ginga, RXTE, CGRO/COMPTEL, GRANAT/SIGMA, and more recently by Chandra, XMM/Newton, along with INTEGRAL. Previous analyses of INTEGRAL data showed that, up to 100 keV, a large fraction of the total emission from the inner Galaxy is due to point sources, and the diffuse emission associated with the Galactic ridge is only

---

<sup>1</sup>Université de Toulouse, UPS-OMP, IRAP, Toulouse, France

<sup>2</sup>CNRS, IRAP, 9 Av. colonel Roche, BP 44346, F-31028 Toulouse cedex 4, France

<sup>3</sup>Max-Planck-Institut für extraterrestrische Physik, Postfach 1603, 85740 Garching, Germany

<sup>4</sup>Hansen Experimental Physics Laboratory, Stanford University, Stanford, CA 94305

one tenth of the total Galactic emission in the 25–100 keV band (Lebrun et al. 2004; Strong et al. 2004; Bouchet et al. 2005, 2008). These analyses also showed that the diffuse emission dominates the hard X-ray sky above 300 keV.

Continuum emission of a diffuse, interstellar nature is expected in the hard X-ray and  $\gamma$ -ray regime from several physical processes: positron annihilation (through intermediate formation of positronium), inverse-Compton (IC) scattering of the interstellar radiation field (ISRF) and bremsstrahlung on the interstellar gas from cosmic-ray (CR) electrons and positrons, and via decay of neutral pions produced in interactions of CR nuclei with the interstellar gas. Extensive studies of the Galactic diffuse  $\gamma$ -ray emission in the context of CR propagation models have been carried out by, e.g., Strong et al. (2000, 2004, 2010) and Strong (2010).

In the present analysis, the data accumulated by the SPI spectrometer onboard the *INTEGRAL* observatory are used to derive the spatial morphology and the spectral shape of the Galactic diffuse emission, taking advantage of the greatly increased observational data and significant advances in the analysis techniques. This builds on our previous work, described in Bouchet et al. (2008) and Porter et al. (2008), where we have presented sky maps and spectra of the Galactic plane and demonstrated the presence of a hard power-law continuum emission, which was interpreted as IC emission from CR electrons and positrons upscattering the Galactic ISRF. For further introductory material and background information on this topic we refer the reader to these earlier papers.

## 2. Instrument and observations

The European Space Agency’s *INTEGRAL* observatory was launched from Baïkonour, Kazakhstan, on 2002 October 17. The SPI spectrometer (Vedrenne et al. 2003) observes the sky in the 20 keV to 8 MeV range with an energy resolution ranging from 2 to 8 keV. It consists of an array of 19 high-purity germanium detectors operating at 80 K. Its geometric surface area is 508 cm<sup>2</sup> with a thickness of 7 cm. In addition to its spectroscopic capabilities, SPI can image the sky with a spatial resolution of  $\sim 2.6^\circ$  (FWHM) over a field of view (FoV) of  $30^\circ$ , because of a coded mask located 1.7 m above the detector plane. Despite this modest angular resolution, it is possible to locate intense sources with an accuracy of a few arc minutes (Dubath et al. 2005). The assembly is surrounded by a 5 cm thick bismuth germanate shield, which stops particles arriving from outside the field of view and measures their flux. The instrument’s in-flight performance is described in Roques et al. (2003). Because of the small number of detectors, SPI’s imaging capability relies on a specific observational strategy, which is based on a dithering procedure (Jensen et al. 2003): the pointing direction varies around a target in steps of  $\sim 2^\circ$  within a five-by-five square or a seven-point hexagonal pattern. In general, a pointing lasts between 30 and 60 minutes, and along its 3 day orbit, *INTEGRAL* operates  $\sim 85\%$  of the time outside Earth’s radiation belts. We have analysed observations recorded from February 22, 2003 through January 2, 2009, covering the entire sky.

## 2.1. Data selection and preparation

We exclude data taken during viewing periods (exposures) that have high background contamination or are dominated by short transient sources which are not useful for our study of the diffuse emission. For example, viewing periods containing solar flares and periods when the spacecraft enters the radiation belts are excluded from the analysis in order to remove periods when the data were dominated by high backgrounds. For energies around 1 MeV, high-energy particles saturate the electronics and can generate false triggers. However, it is possible to use these data thanks to other electronics (via Pulse Shape Discriminators or PSDs) not affected by the saturation problem. These electronics operate in parallel to the fast pre-amplifier output, generating an independent trigger for photon energies between 650 keV and 2.2 MeV. The trigger signal issued by the PSD electronics is used to confirm and select events between 650 keV to 2.2 MeV. The procedure is explained in more detail in Jourdain & Roques (2009).

A further selection based on the  $\chi^2$  between the sky model and the data was made. For a few viewing periods the sky modelling does not correspond very well with the data. This is due to the point-source treatment:

some very short transient sources that are difficult to identify are missed in our sky model and/or there is inaccurate modelling of source variability (see Sec. 3.2.1).

The affected viewing periods, which have relatively high  $\chi^2$  values, contribute only to the systematics for the sky model and hence do not bring useful information on the diffuse emission. These viewing periods account for only  $\sim 2\%$  of the whole dataset. Therefore, we do not use those exposures in the present analysis. After their removal, the dataset contains 38699 exposures for the analysis below 650 keV, which corresponds to a livetime of  $\sim 1.1 \times 10^8$  s. For analysis above 650 keV, the PSD electronics did not operate during some of the viewing periods. Therefore, we also excluded these viewing periods, with the total number in our data set for this energy range then further reduced to 36486. The global  $\chi^2$ , and the maximum  $\chi^2$  per pointing, are given in table 1 for the best model (see Sec. 4.2).

The data contained in the 196–200 keV and 1336–1342 keV band correspond to strong instrumental background lines and are not used in the analysis.

The first band contains the 198 keV line due to the de-excitation of an isomeric state of  $^{71}\text{Ge}$ . The second band contains the 1337 keV line related to  $^{60}\text{Ge}$  K-shell electron capture, which may blend with the 1333 keV  $^{60}\text{Fe}$  line. We bin the data between 20 keV and 2.4 MeV into 24 energy bands for the spectral analysis, and into 7 large energy bands for imaging or diffuse continuum morphology analysis. For the latter analysis, the data contained in the 1170–1176, 1330–1336 and 1806–1809 keV band are removed because they contain counts from the  $^{60}\text{Fe}$  and  $^{26}\text{Al}$  radioactive lines (see Sec. 6).

### 3. Data analysis

The signal recorded by the SPI camera on the 19 Ge detectors is composed of contributions by each source (point-like or extended) in the FoV convolved with the instrument response (see Appendix A), plus the background. For  $N_s$  sources located in the FoV, the counts  $D_p^d$  obtained during an exposure (pointing)  $p$  in detector  $d$  for a given energy band, can be expressed by the relation

$$D_p^d = \sum_{j=1}^{N_s} R_{p,j}^d S_{p,j} + B_p^d \quad (1)$$

where  $R_{p,j}^d$  is the response of the instrument for the source  $j$ ,  $S_{p,j}$  is the flux of the source  $j$ , and  $B_p^d$  is the background recorded of the pointing  $p$  for detector  $d$ . For a given pointing  $p$ ,  $D_p^d$ ,  $R_{p,j}^d$ , and  $B_p^d$  are vectors of  $N^d$ , here 19, elements. For a given set of  $N_p$  exposures, we have to solve a system of  $N_p \times N^d$  equations (Eq. 1). For extended/diffuse sources, we assume a spatial morphology given by an analytic function or a model sky map. To reduce the number of free parameters related to the background, we take advantage of the stability of relative count rates between detectors to rewrite the background term as

$$B_p^d = A_p \times U^d \times t_p^d \quad (2)$$

where  $A_p$  is a normalisation coefficient per pointing related to the background intensity,  $U^d$  represents the background count rate pattern on the SPI camera for the  $d^{th}$  detector ( $U^d$  is a 19-element vector), and  $t_p^d$  is the effective observation time for pointing  $p$  and detector  $d$ . The number of parameters necessary to model the background reduces to  $N_p$  [ $U$  is assumed to be known and can be, in some cases, determined independently from “empty field” exposures (see Sec. 3.1)].

The number of free parameters in the set of  $N_p \times N^d$  equations is then  $N_p \times N_s + N_p$  (for the  $N_s$  sources and the background intensities). An additional reduction of the number of parameters can be obtained because many sources vary on timescales larger than the exposure timescale. Furthermore, many point sources are weak enough to be considered as having a constant flux within the statistical errors, especially for higher energies. Then the  $N_p \times N_s$  parameters related to the sources are reduced to  $N_s^{eff}$  parameters. For example, in the 25–50 keV range, for 257 sources and 38699 pointings,  $N_s^{eff} \simeq 22500$  “time bins” .

#### 3.1. Background

The modelling of the instrumental background is an important issue and challenge for the data analysis. The distribution of the instrumental background in the detector plane changes significantly during the period spanned by the observations because 2 detectors failed early in the

mission (detector 2 on December 7, 2003 and detector 17 on July 17, 2004). The “uniformity” map or background pattern (Eq. 2) should ideally be derived from “empty field” observations. However, the dedicated *INTEGRAL/SPI* “empty fields” are too rare to derive suitable and precise “uniformity” maps for the large dataset used in the present analysis. Another way to determine the background pattern is to solve Eq. 1 for the intensities of both sources, background, and detector pattern simultaneously.

The resulting patterns are therefore model dependent because of the unavoidable cross-talk between the extended source emission and the background pattern (and sources). These effects have been intensively studied above and around 500 keV, where many high latitude exposures can be considered as “empty field” exposures (see Bouchet et al. 2010) because they contained no detectable sources.

For the present study this has a minor impact because the sky model is sufficiently well approximated and hence the derived intensities are not significantly affected.

We treat the background intensity as varying with time and test several timescales. Timescales above 6 hours give poor  $\chi^2$ . In general, the F-test shows that using a background intensity,  $A_p$  (Eq. 2), which varies on an exposure timescale ( $\sim 2800$  s), 2 or 4 hours does not improve the fit compared to using a background timescale of  $\sim 6$  hours. The  $\sim 6$  hours timescale analysis also produces slightly reduced error bars because there are less free parameters for background and source components. However, the intensities are perfectly compatible with those obtained with a more variable background (timescale  $< 6$  hours). We therefore use a background timescale of  $\sim 6$  hours throughout the following analysis.

Finally, the standard configuration used for the analysis consists of computing the background pattern per period between two detector annealings (performed every  $\sim 6$  months to restore the detector energy resolution) with an intensity normalisation that varies with a 6-hour timescale (leading to  $\sim 6000$  intensities to be fitted for the 38699 exposures).

### 3.2. Sky modelling

The data contains contributions from point sources, positron annihilation radiation (511 keV line plus positronium continuum) and from the process of interest in this study, the “diffuse” (non-annihilation) continuum emission, in addition to backgrounds. To extract the diffuse flux with SPI, information for the source positions along with their variability timescales is required. We therefore need to build a sky model to derive the corresponding fluxes.

### 3.2.1. Point-source emission

We follow a similar method to that described in Bouchet et al. (2008) where the point-source contributions are simultaneously extracted together with the diffuse and background components. For each source, the algorithm divides the total observation time into smaller time intervals, down to the exposure duration, where the source can be considered to have a constant flux. The algorithm, based on signal segmentation (Scargle 1998), can detect localised time structures and generally characterise intensity variations. It allows the construction of “time bins” intervals for each source and energy band. The *a priori* information can thus be introduced in the source terms through their position and variability timescales. The intensities in these “time bins” are parameters to be fitted. The catalogues derived in this way optimise the signal-to-noise ratio of both sources and diffuse emission.

However, it is difficult to take into account all transient sources, especially on the shortest timescales (Bird et al. 2010). The information about precise burst locations in time were not available at the time of this analysis and/or is difficult to deduce from the data directly in a blind search. The consequence of missing these sources is to reduce slightly the number of exposures used here, because exposures that are not well fit are excluded from the final dataset (see Sec. 2.1).

The resulting *INTEGRAL/SPI* all-sky survey allows us to identify 254 point sources in the 25–50 keV energy band, with 123, 53, and 26 of the point sources identified at in the lower energy band still emitting in the 50–100, 100–200, and 200–600 keV bands, respectively. See Tables 1 and 2. Figure 2 shows the 50–100 keV all sky map.

For the spectral analysis, a given source is considered to emit as long as its spectrum is detected above  $1\sigma$ . Table 2 gives the number of point sources used to model the data in the different energy bands. More details on the point-source analysis will be given in a forthcoming paper, while in the present work we focus on the diffuse emission.

### 3.2.2. Annihilation radiation spectrum

Between 250 keV and 511 keV annihilation radiation is the dominant emission process with two components associated with the Galactic bulge and disk. We assume that the spatial morphologies for the Galactic bulge annihilation line and positronium continuum are the same. The bulge morphology is described by a combination of  $3.2^\circ$  and  $11.8^\circ$  Gaussians centred at  $l = -0.6^\circ$  and  $b = 0.0^\circ$  with the ratio of the  $11.8^\circ$  to the  $3.2^\circ$  Gaussian flux fixed to 2.16 (Bouchet et al. 2010). For the disk, we follow the Bouchet et al. (2010) modelling for the 511 keV line emission using either a 240  $\mu\text{m}$  NIR/DIRBE<sup>5</sup> map or a halo morphology (see also Weidenspointner et al. 2008; Churazov et al. 2010). Note that in the present analysis we are performing a similar analysis to

---

<sup>5</sup><http://lambda.gsfc.nasa.gov>

that described in Bouchet et al. (2010), but over a wider energy range for the annihilation radiation line and ortho-positronium continuum emission.

The bulge spatial morphology is sufficiently distinct from the diffuse continuum (plus annihilation disk) spatial morphology to be extracted separately from the data, without suffering from “cross-talk”. On the other hand, the disk annihilation continuum is weak compared to the ridge emission and too close in spatial shape to be distinguishable. Consequently, the disk contribution cannot be directly measured, but only inferred from the diffuse continuum measurements (Sec. 6).

### 3.2.3. “Diffuse” emission

To derive the spatial morphology of the diffuse emission (diffuse continuum and annihilation radiation), we use two approaches. The first is sky “imaging” and the second involves sky model fitting.

For “imaging”, sky pixels containing the flux of the diffuse emission (sum of annihilation radiation plus diffuse continuum) are built. The point source locations are then introduced separately as *a priori* information (Bouchet et al. 2008). Intensities of both diffuse pixels and point sources are parameters to be fitted.

For sky model fitting, several parameterised model distributions representing the annihilation radiation spectrum and diffuse continuum emission are directly tested against the data. The spatial morphology of the annihilation radiation spectrum, diffuse continuum emission, and point source locations are introduced separately as *a priori* information. Intensities and fluxes for all the components are parameters to be fitted.

In both cases, sky parameters and background intensities, along with detector patterns, are fitted to the data through the response matrix to maximise the likelihood function.

## 3.3. Core algorithm

The tools used for background modelling, imaging, and model fitting were specifically developed for the analysis of SPI data and described in Bouchet et al. (2008). To determine the sky model parameters we adjust the data through a multi-component fitting algorithm, based on the likelihood test statistic. The core algorithm to handle such a large, but sparse, system is based on MUMPS <sup>6</sup> (Amestoy et al. 2006) together with an error computation method dedicated and optimised for the *INTEGRAL/SPI* response matrix structure (Rouet 2009; Tzvetomila 2009).

---

<sup>6</sup>MUMPS (MULTifrontal Massively Paralell Solver) software developed by the *IRIT/ENSEEIH*T laboratory (<http://mumps.enseeiht.fr>)

## 4. “Diffuse” continuum analysis results

### 4.1. Galactic Emission Spatial Morphology

To determine the (model independent) spatial distribution of the Galactic Ridge emission, the entire sky is divided into pixels. The sky exposure (Fig. 1) is extremely non-uniform. To compensate, the pixels are chosen to have different sizes in latitude and longitude to extract fluxes with a comparable signal-to-noise ratio in each pixel over the whole sky. Because the point sources intensities are derived simultaneously, the pixel sizes also have to be chosen large enough to avoid “cross-talk” with point sources. The region  $|l| < 100^\circ$ ,  $|b| < 30^\circ$  is divided into cells of size  $\delta l \times \delta b = 15^\circ \times 2.6^\circ$  ( $40^\circ \times 5.5^\circ$  for the 600–1800 keV band). Outside of this region, the pixels have a larger sizes depending on their locations. The pixel sizes are chosen *a posteriori* to optimise the signal-to-noise ratio per cell while being sufficiently small to follow the observed diffuse spatial variations. The number of unknowns (the diffuse part of the sky to be “imaged” contains 201 pixels for  $E < 600$  keV and 121 pixels above) is high but reasonable compared to the available data, and the problem is easily tractable using a simple likelihood maximisation to determine all the corresponding intensities and error estimates. For this particular analysis, the fitted intensities are constrained to be positive. This constraint stabilises the “imaging” system of equations to be solved. Figure 3 shows the all-sky intensity images of the diffuse emission in several energy bands. These images and profiles give a qualitative view of the diffuse emission, but very localised structures outside the region delimited by  $|l| > 100^\circ$  and  $|b| > 30^\circ$  may be missed, due to the sizes of the pixel in this region  $\delta l \geq 15^\circ \times \delta b \geq 5.2^\circ$ .

To quantify more easily the behaviour of the diffuse emission, we present our results in terms of longitude and latitude profiles in Fig. 4 and 5. These figures are obtained by integrating the flux measured for  $|b| \leq 6.5^\circ$  in longitude or  $|l| \leq 23^\circ$  in latitude, and  $|b| \leq 8.2^\circ$  and  $|l| \leq 60^\circ$  for the 600–1800 keV band.

Because the images and profiles have a low signal to noise ratio, in order to have more quantitative measurements, a complementary analysis was performed in which the diffuse continuum spatial morphology is modelled using several template maps (table 3), separately or in combination.

Several DIRBE emission maps have been tested as a tracer of the diffuse emission: the NIR/DIRBE (1–10  $\mu\text{m}$ ) related to the stellar emission, the MIR/DIRBE map (10–30  $\mu\text{m}$ ) related to dust nanograins and PAHs heated to high temperatures, and the FIR/DIRBE (30–240  $\mu\text{m}$ ) related to  $\sim$  micron sized dust grains emitting in thermal equilibrium with the heating Galactic ISRF. We have also tested 21-cm H I (Dickey & Lockman 1990) and  $^{12}\text{CO}$  (Dame, Hartmann & Thaddeus 2001) maps. The CO template traces the molecular gas of the Galaxy (which can be related to the distribution to the young stellar populations), and are used to represent the spatial distribution for the nucleosynthesis lines.

Our analysis employs extinction-corrected IR maps, where the method is described in Krivonos et al. (2007) which produces corrected maps to an accuracy of  $\sim 10\%$ . We denote these maps as  $A_\lambda$  where

$\lambda$  is the wavelength. For example, the  $A_{4.9\mu\text{m}}$  map is motivated by the probable stellar origin for the Galactic ridge emission below 100 keV (Krivonos et al. 2007).

The IC maps are based on a physical model for the IC emission generated with the GALPROP code (Sec. 5.1). Note that the IC map spatial morphology is energy dependent, whereas the spatial morphology for the other templates is independent of energy band.

All template skymaps are convolved with the instrument response and compared to the data. The resulting fit parameters are given in table 3.

If a single template is fitted (with intensity as free parameter), the IC templates (models 54z04LMS or 54z04LMS-efactor, described in Sec. 5.3) are the best tracer for the spatial distribution of the diffuse continuum. They provide a better fit to the whole-sky distribution because they account for the emission at high latitudes, but are not always the best fit in the ridge region, where the NIR/DIRBE maps fit the emission better. The best non-IC map is the  $A_{4.9\mu\text{m}}$ , especially for the low energy range ( $E < 200$  keV), consistent with the results of Krivonos et al. (2007) who found that this map traces the diffuse stellar emission distribution at low energies. The IC templates constitute the best model of the whole sky “diffuse” emission, but our derived map contains some unresolved source component in the ridge region. Therefore, an additional second map is needed to model more accurately the excess in the region  $|b| < 10^\circ$ .

Above 600 keV, the IC map fits the data very well, although a marginally better fit can be obtained with the  $1.25 \mu\text{m}$  map. However, the improvement over the IC map is small and is restricted to this energy range. A combination of IC and  $1.25 \mu\text{m}$  maps is also marginally a better fit to the data in the 600–1800 keV band. But, as similarly for the other possible combinations of maps, does not really improve the fit, considering the number of extra degrees of freedom introduced. Furthermore, when the maps are combined the contribution of each separate map is difficult to measure, due to both the statistics and/or the unavoidable “cross-talk”. So, above 600 keV, qualitatively, the best diffuse spatial emission model is the IC map.

At energies below 600 keV, the situation is more complex. In addition to the diffuse continuum, the annihilation radiation component is modeled as described in Sec. 3.2.2. A single IC map is not sufficient to fit the rest of the emission distribution, because it does not fit well the peak along the Galactic plane. An additional map such as DIRBE, CO, or HI is needed to reproduce this structure. Table 3 indicates that below 600 keV, better fits to the spatial morphology emission can be obtained by combining two maps. For the 25–600 keV band, a combination of IC and the  $4.9 \mu\text{m}$ ,  $3.5 \mu\text{m}$  or  $A_{4.9\mu\text{m}}$  map gives the best fits. For the 25–50 keV band an overall best fit can be obtained with a combination of IC and the  $4.9 \mu\text{m}$  maps. This is consistent with the stellar origin for the Galactic ridge emission in the X-ray domain proposed by Krivonos et al. (2007).

Based on these results, and to simplify the statistical analysis, the emission profiles are finally fitted with a combination of the  $A_{4.9\mu\text{m}}$  plus IC and bulge maps below 600 keV, and with a pure IC map above 600 keV, see Figs. 4 and 5, and table 3. With this method the signal-to-noise ratio of the derived diffuse total emission is optimised. Using the absolute best-fit model for each narrow

energy band (bold-italic in table 3) instead of the above adopted model (bold in table 3), does not change the results significantly.

## 4.2. Galactic Ridge Spectral Analysis

In the previous section we considered the spatial morphology and choice of skymap templates. We now turn to the spectral analysis. To extract spectra, we fix the sky model so that the diffuse spectrum morphology below 732 keV (the relevant upper spectral channel above 600 keV), is modelled with a linear combination of  $A_{4.9\mu\text{m}}$  and an IC map computed using GALPROP, plus two Gaussians representing the bulge annihilation radiation component. For energies above 732 keV, the morphology is modelled by the IC map plus 3 spectral lines (Sec. 6). The intensities of the spatial components related to the diffuse emission together with sources and background intensities are adjusted to the data as described in Sec. 3.3.

Details on the individual component separation procedure are given in Appendix A. The bulge morphology differs significantly from the  $A_{4.9\mu\text{m}}$  and IC map components and there is very little “cross-talk”, hence this component is easily extracted separately (Table 4a). On the other hand, IC and  $A_{4.9\mu\text{m}}$  components are more difficult to disentangle due to their rather similar morphologies. Nevertheless, it is possible to separate the contribution of each map (Table 4b-c). To take into account the “cross-talk” between the IC and  $A_{4.9\mu\text{m}}$  components, we add, in addition to statistical errors on fluxes, artificial systematic errors<sup>7</sup>. When deriving these components, the data above  $\sim 1$  MeV are not used because the lower statistics do not allow for the distinction. The IC and  $A_{4.9\mu\text{m}}$  spatially-derived maps are then fitted as a superposition of three expected physical spectral components:

- Emission by “unresolved sources”, dominating below  $\sim 50$  keV, modelled by an exponential cutoff power-law spectrum.
- Annihilation radiation spectrum modelled using a Gaussian centered at 511 keV with 2.5 keV FWHM plus positronium continuum (Ore & Powell 1949).
- Diffuse continuum mainly attributed to interstellar emission, modelled by a power law.

The diffuse spectral fitted parameters following the above procedure for the central radian defined by  $|l| < 30^\circ$ ,  $|b| < 15^\circ$  are given in table 4.

---

<sup>7</sup> The reduced  $\chi^2$  between the data and the model is abnormally high ( $\chi^2 > 2$ ) and technically XSPEC (v11) spectral fitting code does not compute the standard deviation of the fitted parameters. “Cross-talk” produces data fluctuations that are not statistical; systematic errors are then added to statistical errors. Adding 25 % systematic error in XSPEC gives a reduced  $\chi^2$  of about 1. These systematic mainly increase errors bars below 100 keV.

The IC extracted component is found to have a power-law index  $\sim 1.8$  with a 100 keV flux  $9 \times 10^{-5}$  ph cm $^{-2}$  s $^{-1}$  keV $^{-1}$ . The A $_{4.9\mu\text{m}}$  tracer component is found to have a much harder power-law index of  $\sim 1$  with an intensity significantly lower than the IC component. In other words, the IC component dominates the flux over the sky. For the full sky, the ratio of IC to A $_{4.9\mu\text{m}}$  components is 14, 8, 1.8 and 0.95 at 50, 100, 500 and 1 MeV, respectively. When considering only the central radian, the IC component contains 15% at 20 keV rising to 25% at 1 MeV of the total IC sky flux. The 20–100 keV flux ratio of IC to A $_{4.9\mu\text{m}}$  component is  $\sim 9$  for the whole sky and 2.6 for the central radian.

The final fit is made for the total spectrum (sum of all components) by combining the spectral information obtained from each spatial morphology component fit. For this step, the A $_{4.9\mu\text{m}}$  and IC power-law indices and intensities are fixed while fitting the other components. We also introduce a cutoff in the A $_{4.9\mu\text{m}}$  component to steepen its contribution at higher energies (above 1 MeV) where it would be inconsistent with the data from the higher energy instruments otherwise. We model the component related to unresolved sources with a single exponential cutoff spectrum. If the summed spectral components for IC, A $_{4.9\mu\text{m}}$ , and annihilation radiation are directly decomposed into the three spectral components described above, then the resulting spectral shape is similar to that described in the previous paragraph. The interstellar emission component is then best fit by a power-law of index  $\sim 1.4$ -1.5. It results in a diffuse continuum spectrum very similar to that of the summed power laws of the IC and A $_{4.9\mu\text{m}}$  components. The total diffuse spectrum for the central radian region is presented in Fig. 6.

These results are consistent with our previous work (Bouchet et al. 2008), except that the diffuse continuum power law obtained with the IC maps has a higher intensity (20–30% at 50 keV). This is due to the large latitude extent of this model which contributes significant integrated flux very far from the Galactic ridge, and not included in Bouchet et al. (2008).

Above 1 MeV, the decomposition of the emission into two spatial components gives too much uncertainty for each component. We therefore show our determination of the diffuse emission based on estimating a minimum and maximum extracted intensity for each component. To do this we fitted the spatial morphology with the A $_{4.9\mu\text{m}}$  tracer, which gives nearly the minimum extracted flux, while the IC map gives the maximum extracted flux. A similar spectral analysis as that described above was then performed. The range of uncertainty is shown as a shaded area in Fig. 6.

### 4.3. Diffuse emission contamination with extragalactic background emission

The conventional coded-mask system provides, by construction, flux free from extragalactic background (EGB) contamination, but for INTEGRAL/SPI we need a background model (see Sec. 3.1). Due to the background modelling there is uncertainty associated with the level of diffuse extragalactic background (EGB) flux in our diffuse emission determination. The instrument background is modelled with a background pattern whose intensity varies on a  $\sim 6$  hours time scale

(Sec. 3.1). Alternatively, it can also be modelled as above but with an additional isotropic term, which can be either stable in time (to represent the EGB) or variable in time (related to long term variations of the background component). Nevertheless, it is difficult to distinguish between the two, and the first one is preferred for its simplicity.

In our analysis, for the region  $|l| \leq 30^\circ$  and  $|b| \leq 15^\circ$  we find that EGB contamination is negligible ( $< 3\%$ ) below 600 keV. For energies above 600 keV, because of the lower statistics, if we assume that the measured diffuse emission is EGB-dominated, then the diffuse component is reduced by at most  $\sim 28\%$  in the region  $|l| < 30^\circ$  and  $|b| < 15^\circ$ . This is within the error bars and does not affect our conclusions associated with the modelling (see below).

## 5. Modelling the diffuse emission

### 5.1. GALPROP models

The GALPROP code (Strong & Moskalenko 1998; Strong et al. 2000, 2004, 2007) including a new model for the Galactic interstellar radiation field (ISRF) is the basis for predicting Galactic diffuse emission in the energy range from keV to TeV energies, thus covering more than 10 orders of magnitude in energy (Porter et al. 2008). The goal of the GALPROP project is to combine CR and broadband diffuse emission data from radio to  $\gamma$ -rays into a single interpretative framework. Therefore, while the modelling and interpretation has most recently focussed on  $\gamma$ -ray data from the *Fermi* mission, it is also applicable to other experiments like *WMAP*, *PLANCK*, *INTEGRAL* and *MILAGRO*.

In Porter et al. (2008) we used the so-called “EGRET-excess” based model (Strong et al. 2004), which invoked CR proton and electron spectra different from those measured directly in the Solar System, in order to account for the  $\gamma$ -ray spectrum measured by *EGRET*. Now that the “GeV excess” in this spectrum has been shown to be absent in *Fermi-LAT* data (Abdo et al. 2009), being presumably an *EGRET* instrumental effect, we use in the present work the “conventional model”, which requires consistency of the modelled CR intensities and spectra with those directly measured. We use the model (GALPROP ID 54\_z04LMS) described in Strong et al. (2010), which reproduces the electron (plus positron) spectrum measured by *Fermi-LAT* (Abdo et al. 2010), but is not fitted to *Fermi-LAT*  $\gamma$ -ray data. It has a halo height of 4 kpc and includes CR reacceleration; for further details see Strong et al. (2010).

The calculations presented in Strong et al. (2004), Porter et al. (2008) and Strong et al. (2010) show the importance of secondary leptons in CRs for the proper calculation of the diffuse emission. Secondary CR positrons and electrons produced via interactions of energetic nucleons with interstellar gas are usually considered as a minor CR component. However, the secondary positron and electron flux is comparable to the primary electron flux around  $\sim 1$  GeV in the ISM, providing diffuse emission in addition to that from primary CR electrons. The enhancement is  $\sim 1.2 - 1.4$

times higher in the IC  $\gamma$ -rays up to MeV energies relative to that from pure primary electrons. This leads to a considerable contribution of secondary positrons and electrons to the diffuse  $\gamma$ -ray flux via IC and bremsstrahlung and to a significant increase of the Galactic diffuse flux below 100 MeV. For a detailed breakdown of the primary and secondary leptonic components as a function of energy see Porter et al. (2008) and Strong et al. (2010). Secondary positrons and electrons are, therefore, indirectly traced by hard X-rays and  $\gamma$ -rays. The spectrum of secondary positrons and electrons depends only on the ambient spectrum of nucleons, the interstellar gas, and the adopted propagation model<sup>8</sup>. Figure 7 show the components of the ISRF that contribute to the IC emission in different energy ranges. The scattering of optical photons provides the majority contribution for  $\gtrsim 10$  MeV, while the far-infrared dominates in the  $\sim 0.1 - 10$  MeV range, and the CMB is dominant below  $\sim 0.1$  MeV.

## 5.2. Comparison of SPI spectrum with GALPROP models

Figure 7 compares our baseline GALPROP model with the spectrum measured by SPI. The agreement with the spectral shape is reasonable but the overall intensity is slightly lower than the data. Better agreement with the SPI data is obtained by considering a model with a higher normalisation for the primary electron spectrum, which is illustrated in Fig. 8 where the total electrons are increased by a factor of 2 over the baseline model. An interpretation for this increase can be that the locally-measured spectrum is not typical of the global average at the solar position, or that the CR source distribution is more peaked toward the inner Galaxy than that used in the baseline model. Alternatively, Fig. 9 shows other possibilities to increase the IC component, either by increasing the Galactic CR halo height from 4 kpc to 10 kpc, or by increasing the input luminosity of the bulge component for the ISRF by a factor of 10. The uncertainty associated with the bulge input luminosity, metallicity gradient, and other factors all contribute so that the ISRF in the inner Galaxy is not as constrained as observed locally. Currently, the radial distribution of CR sources is not well known or constrained, and a factor 2 increase of the electrons in the inner few kpc is possible. The same effect could be obtained with secondary CR positrons and electrons if their CR nuclei progenitors were increased by a similar factor, but then this could be inconsistent with the diffuse  $\gamma$ -ray emission measured by the *Fermi-LAT* which is mainly produced by the same CR nuclei. A larger halo is suggested by analysis of CR data (Trotta et al. 2010) and  $\gamma$ -rays (Strong 2010). Unfortunately, the morphology of these components is not distinguishable by *INTEGRAL/SPI* over the spatial region currently covered. Future observations at higher latitudes would allow discrimination between the different halo/enhanced ISRF combinations, but this will be the subject of future work.

---

<sup>8</sup>The discovery of enhanced positron fluxes above 10 GeV by the PAMELA instrument is not of importance here since, despite this component, at those energies primary electrons fully dominate the lepton fluxes.

### 5.3. Comparison of IC spectrum with template-fitted spectrum

As a further check we compare power-law approximations of the GALPROP models with those derived from template fitting. The best power-law fit to the GALPROP model spectrum shown in Fig. 7 (ID 54 z04LMS) is  $N(E) = 0.16 \times E^{-1.76}$ , where  $E$  is the energy in keV. The power-law fit to the SPI-extracted IC template is  $N(E) = 0.34 \times E^{-1.79}$ , which is two times higher than the GALPROP model intensity. For the model shown in Fig. 8 (model 54\_z04LMS\_efactorS, which has the primary electrons increased by a factor 2), the best power-law fit to the model in the range 20 keV–5 MeV is  $N(E) = 0.29 \times E^{-1.76}$ . Meanwhile, the power-law fit to the SPI-extracted IC template is now  $N(E) = 0.30 \times E^{-1.76}$ , which is completely consistent with the model spectrum. Similar results can be obtained for the other models involving modifications to the CR confinement volume, or the intensity of the ISRF in the inner Galaxy. Thus, it seems that at least some enhancement in the inner Galaxy is required for the diffuse emission, but it can be due to a combination of effects. These we will explore in subsequent work.

### 5.4. Electron energies probed by the SPI data

The photon energy range from 50 keV to 2 MeV is sensitive to IC from electrons below about 5 GeV. To illustrate this, Fig. 10 shows GALPROP model calculations as in Fig. 7, but for primary electron source spectra cutoff below 1 GeV and 5 GeV, respectively. The 5 GeV cutoff removes most of the emission in the SPI range, which comes mainly from CMB and far-infrared component of the ISRF. With the 1 GeV cutoff much of the emission is restored, showing that most of the IC in the energy range considered in this paper comes from electrons between 1 and 5 GeV. For these energies, the locally measured CR electron spectrum is strongly affected by heliospheric modulation and the SPI measurements can allow direct probing of the *interstellar* spectrum of these CRs. In turn, understanding the heliospheric transport of CRs could be improved because uncertainties on the true interstellar CR spectra directly affect the heliospheric model predictions.

## 6. Non-IC diffuse components :<sup>26</sup>Al, <sup>60</sup>Fe lines and annihilation radiation emission

The main focus of this paper is continuum emission, so for the lines and positronium we restrict ourselves to a check on the consistency of our global diffuse spectrum, because these components are extracted simultaneously. These topics will be explored in greater detail in a separate paper.

The <sup>26</sup>Al line has been shown to be intrinsically narrow with an  $2\text{-}\sigma$  upper limit on the width of less than 1.3 keV (Wang et al. 2009). To take into account the emission of this diffuse line, we use an energy band from 1806 keV to 1812 keV. The line is strong compared to the continuum flux in this band and is essentially unaffected by the assumed underlying power law parameters and diffuse continuum spatial shape. The contribution in counts of this line through its interaction

with the detectors (Compton effect, etc.) was subtracted from the continuum prior to the diffuse continuum data analysis. The  $^{26}\text{Al}$  line is detected at  $\sim 13\sigma$  with a flux of  $3.3 - 3.6 \times 10^{-4}$  ph cm $^{-2}$  s $^{-1}$  in the inner Galaxy ( $|l| < 30^\circ$ ,  $|b| < 10^\circ$ , which agrees with earlier measurements (Wang et al. 2009, and references therein).

The  $^{60}\text{Fe}$  isotope produces two lines at 1173.23 and 1332.50 keV detected, depending on the details of their spatial morphology, at a level of  $\sim 2\sigma$  and  $\sim 3\sigma$ , respectively. Their mean flux in the inner Galaxy is  $\sim 6 \times 10^{-5}$  ph cm $^{-2}$  s $^{-1}$  keV $^{-1}$ . The fluxes derived from this analysis and the  $^{60}\text{Fe}$  to  $^{26}\text{Al}$  ratio of  $\sim 0.17$  agree with those of Smith (2004) and Wang et al. (2007).

The annihilation radiation characteristics have here been measured over a wide energy range. The derived fluxes are consistent with those in the literature, implying a positronium fraction close to 100%, both in the line and the positronium continuum. The bulge to disk ratio flux is  $\sim 0.2 - -0.3$  for the whole Galaxy for both the line and the positronium continuum. For a review on this subject, see Higdon, Lingenfelter & Rothschild (2009).

## 7. Other phenomena in the inner Galaxy

### 7.1. The “Fermi Bubbles”

Using *Fermi-LAT* data, a claim has been made for two large  $\gamma$ -ray “bubbles”, extending  $50^\circ$  above and below the Galactic center, with a width of about  $40^\circ$  in longitude (Su, Slatyer & Finkbeiner 2010). The  $\gamma$ -ray emission associated with these bubbles appears to have a harder spectrum ( $dN/dE \propto E^{-2}$ ) than the  $\gamma$ -rays produced by  $\pi^0$ -decay by CR nuclei interacting with the ISM, or IC emission from CR electrons and positrons modelled using GALPROP. It has also been suggested that the “bubbles” are spatially partly correlated with the hard-spectrum microwave excess known as the *WMAP* haze.

If the features are real, and are associated, the IC  $\gamma$ -ray emission could extend down into the *INTEGRAL/SPI* energy range.

We modelled the “bubbles” using circular regions centred at  $b = 30.5^\circ$  and  $b = -30.5^\circ$  with a radius of  $22^\circ$  having a uniform emissivity, and tested various combinations of the maps (see Table 3) along with the “bubble” templates. For the 25–50 keV range, it is not possible to find an unique combination of maps including the “bubble” template that do not result in it being assigned a negative coefficient in the fit. Imposing the positivity constraint for the fluxes, we find no detection in this energy range, as indicated in the table. Similarly, above 50 keV there is no emission found corresponding to the “bubbles”. The  $2\text{-}\sigma$  upper limits in several energy bands above 50 keV, assuming an emission with a power-law index -2, are given in Table 5.

## 7.2. Connection with past activity in the Galaxy

The increased electron flux in the inner Galaxy could also be related to past activity in the Galactic Centre, as has been proposed for example for X-ray fluorescence (Terrier et al. 2010; Capelli et al. 2011). However this would be much more localised near the Galactic Centre, so that a direct connection seems unlikely. Other more exotic possibilities for increased electron fluxes, like hypernovae (e.g., related to  $\gamma$ -ray bursts) cannot be ruled out with the present data.

## 8. Summary and discussion

New results on the diffuse emission spatial morphology and spectrum in the range 20 keV–2.4 MeV have been obtained from the analysis of 6 years of *INTEGRAL/SPI* data. Over this energy range, what is seen as diffuse emission is the result of the superposition of several physical processes; annihilation radiation, cosmic nuclear  $\gamma$ -ray lines, diffuse continuum due to interstellar emission, and unresolved sources. In the present analysis we have been able to isolate each of these diffuse components. We have explored uncertainties and limitations due to the data reduction along with the spatial morphology modelling.

The diffuse emission intensity in the central radian ( $|l| < 30^\circ$ ,  $|b| < 15^\circ$ ) is estimated to be one tenth of the total emission (including sources) below 100 keV and one third in 100–300 keV band. The diffuse emission spectrum has the following main features:

- The diffuse continuum spectrum (apart from positronium) is fitted by a power law of index 1.4 – 1.5, with a flux at 100 keV of  $1.1 \times 10^{-4}$  ph cm $^{-2}$  s $^{-1}$  keV $^{-1}$ . This power law, thought to be related to interstellar emission, can be decomposed into two spatial components: the IC component with a power law of index 1.8 and a flux at 100 keV of  $\sim 10^{-4}$  ph cm $^{-2}$  s $^{-1}$  keV $^{-1}$  and another component which can be modelled with the an extinction-corrected 4.9  $\mu$ m DIRBE-based template, whose spectral shape is a power law with an index of  $\sim 1$  and a flux at 50 keV of  $\sim 3 - 4 \times 10^{-5}$  ph cm $^{-2}$  s $^{-1}$  keV $^{-1}$ . This additional component is weak below 200 keV compared to the IC component.
- The diffuse continuum flux around 1 MeV is found compatible with the *COMPTEL/CGRO* measurement.
- The IC emission distribution predicted by the GALPROP code is in fair agreement with the data. However, a model with an electron spectrum increased by a factor 2 over the standard model based on the electrons (plus positrons) measured by *Fermi-LAT* is in better agreement. Also, an increased ISRF in the Galactic bulge or a large Galactic CR halo are other reasonable possibilities to that can lead to an increased flux. The data analysed in this paper do not allow a distinction to be made between these possibilities.

- An additional component is required below 50 keV. This excess over the IC emission is well modelled with the NIR/DIRBE 4.9  $\mu\text{m}$  map. This low-energy component has an exponential spectrum with a cutoff at 8 keV and a flux at 50 keV of  $\sim 2 \times 10^{-4} \text{ ph cm}^{-2} \text{ s}^{-1} \text{ keV}^{-1}$ . It can be interpreted in terms of the stellar origin as proposed by Krivonos et al. (2007).

The diffuse continuum emission spectrum obtained with the present analysis confirms and improves on the results reported in Bouchet et al. (2008) and Porter et al. (2008). Below 100 keV, it is also compatible with results obtained from *INTEGRAL/IBIS* analysis (Krivonos et al. 2007; Türler et al. 2010). In addition, we found that our global diffuse spectrum is consistent through the measured characteristics of nuclear lines ( $^{26}\text{Al}$ ,  $^{60}\text{Fe}$ ) and annihilation radiation spectrum.

There is no detection in the SPI energy range of the “Fermi bubbles” at the present level of sensitivity.

The *INTEGRAL/SPI* will continue to provide new data for at least the next 3 years. Meanwhile, the *Fermi-LAT* will be operating at least over this time span, and analysis of its data continues to yield further information on the diffuse  $\gamma$ -ray emission  $\gtrsim 100$  MeV. An analysis showing the complementarity of the data provided by these instruments enabling us to probe the physical processes producing the diffuse emission is given in Strong (2010). Together with existing data from other instruments, the data from these two currently operating missions allows the investigation of the CR electron spectrum at all energies, which will eventually enable an unambiguous decomposition of the diffuse  $\gamma$ -ray sky.

The *INTEGRAL/SPI* project has been completed under the responsibility and leadership of CNES. We are grateful to ASI, CEA, CNES, DLR, ESA, INTA, NASA and OSTC for support.

GALPROP development is partially funded via NASA grants NNX09AC15G and NNX10AE78G.

Some of the results in this paper have been derived using the HEALPix (Górski et al. 2005) package.

## REFERENCES

- Abdo, A. A., Ackermann, M., Ajello, M., et al., 2009, *Phys. Rev. Lett.*, 103, 25, id. 251101
- Abdo, A. A., Ackermann, M., Ajello, M., et al., 2010, *Phys. Rev. Lett.*, 104, 10, id. 10110
- Amestoy, P. R., Guermouche, A., L'Excellent, J. Y., & Pralet, S. 2006, *Parallel Computing*, Vol 32 (2), pp 136-156.
- Bleach, R. D., Boldt, E. A., Holt, S. S., Schwartz, D. A, et al., 1972, *ApJ*, 174, L101
- Bird, A. J., Bazzano, A., Bassani, L., et al., 2010, *ApJS*, 186, 1
- Bouchet, L., Roques, J. P., Mandrou, P., et al., 2005, *ApJ*, 635, 1103
- Bouchet, L., Jourdain, E., Roques, J. P, et al., 2008, *ApJ*, 679, 1315
- Bouchet, L., Jourdain, E., Roques, J. P., et al., 2009, in *Proceedings of The Extreme sky: Sampling the Universe above 10 keV*, <http://pos.sissa.it/cgi-bin/reader/conf.cgi?confid=96>, p.16
- Bouchet, L., Roques, J. P., & Jourdain, E., 2010, *ApJ*, 720, 1772
- Capelli R., Warwick R. S., Porquet D., et al., 2011, *A&A*, 430, A38
- Churazov, E., Sazonov, S., Ysygankov S., et al., 2010, *MNRAS*, in press (arXiv:1010.0864C)
- Dame, T. M., Hartmann, D., & Thaddeus, P., 2001, *ApJ*, 547, 792
- Dickey, J. M., & Lockman, F. J., 1990, *ARA&A* , 28, 215
- Diehl, R., Dupraz, C., Bennett, K., et al., 1995, *A&A*, 298, 445
- Diehl, R., Halloin, H., Kretschmer, K., et al., 2006, *Nature*, 439, 435
- Dogiel, V. A., Schönfelder, V., & Strong, A. W., 2002 *A&A*, 382,730
- Dubath, P., Knödlseeder, J., Skinner, G. K., et al., 2005, *MNRAS*, 357, 420
- Ebisawa, K., Tsujimoto, M., Paizis, A., et al., 2005, *ApJ*, 635, 214
- Górski, K. M., et al., 2005, *ApJ*, 622, 759
- Hands, A. D. P., Warwick, R. S., Watson, M. G., & Helfand, D. J. 2004, *MNRAS*, 351, 31
- Harris, M. J, Knödlseeder, J., Jean, P., et al., 2005, *A&A*, 433, L49
- Higdon, J. C., Lingenfelter, R. E., & Rothschild, R. E., 2009, *ApJ*, 698, 350
- Jensen, P. L., Clausen, K., Cassi, C., et al., 2003, *A&A*, 411, L7

- Jourdain, E. & Roques J. P., 2009, ApJ, 704, 17
- Kaneda, H., Makishima, K., Yamauchi, S., et al., 1997, ApJ, 491, 638
- Krivonos, R., Revnivtsev, M., Churazov, E., et al., 2007, A&A, 463, 957
- Lebrun, F., Terrier, R., Bazzano, A., et al., 2004, Nature, 428, 293
- Mahoney, W. A., Ling J. C., Jacobson, A. S., & Lingenfelter, R. E. 1982, ApJ, 262, 742
- Ore, A. & Powell, J. 1949, Phys. Rev., 75, 1696
- Plüschke, S., Diehl, R., Schönfelder, V., et al., 2001, ESA-SP 459, 55
- Porter, T. A., Moskalenko, I. V., Strong, A. W., et al., 2008, ApJ, 682, 400
- Rouet, F. R. 2009, Partial computation of the inverse of a large sparse matrix- application to astrophysics, INP-ENSEEIHHT/IRIT, <http://rouet.perso.enseeiht.fr/report.pdf>
- Roques, J. P., Schanne, S., Von Kienlin, A., et al., 2003, A&A, 411, L91
- Scargle, D. 1998, ApJ, 504, 405
- Smith, D. M. 2004, ESA-SP-552, 45
- Strong, A. W. & Moskalenko, I. V., 1998, ApJ, 509, 212
- Strong, A. W., Bloemen, H., Diehl, R., et al., 1999, Astrophys. Lett. Commun., 39, 209
- Strong, A. W., Moskalenko, I. V., & Reimer, O. 2000, ApJ, 537, 763
- Strong, A. W., Diehl, R., Halloin, H., et al., 2005, A&A, 444, 495
- Strong, A. W., Moskalenko, I. V., & Reimer, O. 2004, ApJ, 613, 962
- Strong, A. W., Moskalenko, I. V., & Ptuskin, V. S., 2007, Ann. Rev. Nucl. Part. Sci., 57, 285
- Strong, A.W., Proceedings of the ICATPP Conference on Cosmic Rays for Particle and Astroparticle Physics, 2010, to be published by World Scientific (Singapore), arXiv:1101.1381.
- Strong, A. W., Porter, T A., Digel, S. W., Jóhannesson, G., Martin, P., Moskalenko, I. V., Murphy, E. J., & Orlando, E. 2010, ApJ, 722, L58
- Sturmer S. J., Schrader C. R., Weidenspointner, G., et al., 2003, A&A, 411, L81
- Su, M., Slatyer, T. R., & Finkbeiner, D. P. 2010, ApJ, 724, 1044
- Terrier R., Ponti G., Bélanger G., et al., 2010, ApJ, 719, 1 43
- Trotta R. L., Jóhannesson, G., Moskalenko I. V., et al., 2010, ApJ, 729, 106

- Tur C., Heger, A. & Austin, S. M. 2010, *ApJ*, 718, 357
- Türler, M., Chernyakova, M., Courvoisier, T. J.-L., et al., 2010, *A&A*, 512, 49
- Tzvetomila, S. 2009, Parallel triangular solution in the out-of-core multifrontal approach for solving large sparse linear systems, <http://pantar.cerfacs.fr/6-26642-PhD-Dissertations.php>
- Valinia, A., Kinzer, R. L., & Marshall, F. E. 2000, *ApJ*, 534, 277
- Vedrenne, G., Roques, J. P., Schonfelder, V., et al., 2003, *A&A*, 411, L63
- Yamasaki, N. Y., Ohashi, T., Takahara, F., et al., 1997, *ApJ*, 481, 821
- Wang, W., Harris, M. J., Diehl, R., et al., 2007, *A&A*, 469, 1005
- Wang, W., Lang, M. G., Diehl, R., et al., 2009, *A&A*, 496, 713
- Weidenspointner, G., Skinner, G., Jean, P., et al., 2008, *Nature*, 451, 159
- Woosley, S. E., & Heger, A., 2007, *Phys. Rep.*, 442, 269

### A. Form of INTEGRAL/SPI the response matrix

The SPI response  $R$  has been splitted into 3 components which correspond to the detector response to the photopeak events:  $R^{(1)}$ , non-photopeak events that interact first in a detector:  $R^{(2)}$  (Compton interaction, . . .) and photons that interact first in the passive material surrounded the detector:  $R^{(3)}$ .

$$R(E, E_{ph}, \theta, d) = \sum_{i=1}^3 R^{(i)}(E, E_{ph}, \theta, d) \quad (\text{A1})$$

Here  $E$  stands for the detected energy,  $E^{ph}$  for the incident photon energy,  $\theta$  for the incident photon direction relative to the telescope axis and  $d$  the detector number. The templates  $R^{(i)}$  were found to a good approximation to not vary with detector or incident photon direction, only their normalization changes (Sturmer et al. 2003). The templates are thus determined for a given photon energy and only the normalization or efficiency is calculated for every incident photon direction and detector number. In short, each component has been again splitted in two parts. The first part is Imaging Response Function (IRF) and the second part is the Redistribution Matrix File (RMF). The IRFs contain the detector effective area as the function of the detector number ( $d$ ), the incident photon direction ( $\theta$ ) and the incident photon energy ( $E_{ph}$ ). The RMFs contain information about the energy distribution of detector counts ( $E$ ) for photons of a given incident energy ( $E_{ph}$ ). The response is rewritten as:

$$R(E, E_{ph}, \theta, d) = \sum_{i=1}^3 IRF^{(i)}(E_{ph}, \theta, d) \times RMF^{(i)}(E, E_{ph}) \quad (\text{A2})$$

$$\int R(E, E_{ph}) dE = 1 \quad (\text{A3})$$

This decomposition into static components reduces the computation time and storage. More detailed can found in Sturmer at al., 2003.

The detector counts  $C$  produces by a source (incident photon direction  $\theta$ ) emitting a spectrum  $S(E_{ph}, \theta)$  is

$$C(E, d) = \sum_{i=1}^3 \int IRF^{(i)}(E_{ph}, \theta, d) \times RMF^{(i)}(E, E_{ph}) S(E_{ph}, \theta) dE_{ph} \quad (\text{A4})$$

$$= \sum_{i=1}^3 C^{(i)}(E, \theta, d) \quad (\text{A5})$$

For  $N_p$  exposures (or pointings),  $N_d$  detectors,  $N_s$  sources and  $N_e$  energy band (Sec. 3), the equation is

$$C(E, d, p) = \sum_{s=1}^{N_s} \sum_{i=1}^3 \int IRF^{(i)}(E_{ph}, \theta_s, d, s) \times RMF^{(i)}(E, E_{ph}) S(E_{ph}, \theta_s) dE_{ph} \quad (A6)$$

$\theta_s$  is the direction of the source number  $s$  relative to the telescope axis and  $S(E_{ph}, \theta_s)$  its incident photon spectrum.

The number of equations to hold simultaneously is then  $N_d \times N_p \times N_e$  and the number of unknowns is  $N_s \times N_e$ , assuming no background and constant flux sources (Sec. 3).

Taking into account completely the response matrix requires to solve a more complex equation than eqn 1 with extra additional dimensions in both data space (all detected energy or data channels) and photon space (incident photon energy). Fortunately, it is possible to use a close approximation of these equations to reduce it to the form of eq. 1. The latter system of equation is subsequently solved several times (for each energy band), with  $N_d \times N_p$  equations to hold simultaneously and  $N_s$  unknowns.

### A.1. Flux extraction in counts space

To reduce the dimension of the problem to be solved, a flux extraction in counts space is first done and the resulting source counts are then converted into incident photon spectrum. In this case only the photopeak response part is used.

$$C(E, d) = C^{(1)}(E, \theta, d) \times \left(1 + \frac{C^{(2)}(E, \theta, d) + C^{(3)}(E, \theta, d)}{C^{(1)}(E, \theta, d)}\right) \quad (A7)$$

The term  $IRF^{(1)}$  is is photopeak efficiency (and omitting the energy resolution term for simplicity),

$$RMF^{(1)}(E, E_{ph}) = \delta(E, E_{ph}) \quad (A8)$$

$$C^{(1)}(E, \theta, d) = IRF^{(1)}(E, d) \times S(E, \theta) \quad (A9)$$

Then

$$C(E, d) = IRF^{(1)}(E, d) \times S(E, \theta) \times \beta(E, \theta, d) \quad (A10)$$

For a fixed energy  $E$ , making the approximation that whatever the event types, the spatial distribution of counts over the detector plane (in function of the detector number  $d$ ) is similar and hence does not depend on the detector number  $d$  ( $\beta(E, \theta, d) \simeq \beta(E, \theta)$ ), then

$$C(E, d) = IRF^{(1)}(E, \theta, d) \times S(E, \theta) \times \beta(E, \theta) = IRF^{(1)}(E, \theta, d) \times S^{counts}(E, \theta) \quad (A11)$$

Here  $S^{counts}$  is called the flux in counts space.

### A.2. Direct photon flux extraction – “pseudo-efficiency”

It is possible to extract the sources photon spectrum directly from the data. For that the emission spectrum spectral shape is assumed to be known and to be continuous in energy. This shape can for example, be extracted after a first flux extraction in counts space and conversion into incident photon spectrum.  $S^{Fitted}$  being the fitted photon spectrum, then

$$C(E, d) = \frac{\sum_{i=1}^3 \int IRF^{(i)}(E_{ph}, \theta, d) \times RMF^{(i)}(E, E_{ph}) S^{Fitted}(E_{ph}, \theta) dE_{ph}}{S^{Fitted}(E, \theta)} \times S(E, \theta) \quad (A12)$$

If  $S^{Fitted}(E, \theta)$  is sufficiently close to the incident spectrum  $S(E, \theta)$  then the above formula predicts counts in data space. It can be rewritten

$$C(E, d) = R^{Pseudo}(E, \theta, d) \times S(E, \theta) \quad (A13)$$

$R^{Pseudo}$  is the response of the instrument assuming a continuous photon emission spectrum of known spectral shape (for 1 incident photon in each energy band).

### A.3. ‘Simplified’ system of equations

Finally, for  $N_s$  sources located in the field of view, the data  $D(d,p,E)$  obtained during an exposure (pointing p) in the detector d for given energy E is

$$D_{dp} = \sum_{j=1}^{N_s} R_{dp,j} S_{p,j} + B_{dp} \quad (A14)$$

$B_{dp}$  is the background obtained during an exposure (pointing p) in detector d for given energy E. R can be either  $IRF^{(1)}$  or  $R^{Pseudo}$ . The equation will be solve in this latter form (eq. 1).

If the sources emission spectrum follows a known spectral shape, then the counts predicted by the pseudo efficiency method is more realistic. Anyway this method can be more sensitive to errors

in the simulated response matrix and storage simplification made, and requires the knowledge of the incident photon spectrum which might be continuous in energy. In the other hand, the flux extraction in counts space, may predict inaccurate source counts as the photopeak like assumed response is not the true response.

## B. Impact of the energy redistribution matrix form on diffuse measurement

The first approximation (counts flux approximation) used only the photopeak part of the response to obtain fluxes in counts space in a first step. Then, these counts fluxes are then converted into incident photon spectrum. The “pseudo-efficiency” response allows obtaining directly an incident photon spectrum.

For the counts flux approximation, for each point-source a small fraction of the non-photopeak events could have been included in the background or vice-versa. For a given point source, the effect is negligible on the extracted counts spectrum. Nevertheless, for the present analysis and due to the numerous point sources (accumulation effect) and their spatial distribution (most of them located around the Galaxy plane), these counts residuals may sum-up to mimic a false diffuse emission like supplementary component. This effect is visible in fig. 11, actually it is negligible for the whole sky spectrum but is important for the central radian region. It is not the case for the “pseudo-efficiency” approximation as long as a close estimate of each point-source incident photon spectral emission shape is available. The method gives by construction a better extraction of sources counts and separation from other component. Nevertheless, the method is sensitive to errors in the non-photopeak events response matrices.

Figure 11 shows the resulting diffuse spectrum of each components and the the combined spectrum for the two approximations mentioned above plus a third case where the “pseudo-efficiency” is used for point-sources, while photopeak response is used for all the diffuse components. These three analyses were done in parallel at each step of the study. They give an idea of the uncertainties/systematic. All produces compatible results above 100 keV, below a larger intensity is found for the diffuse components as suspected. Anyway, we use results obtain with “pseudo-efficiency” as it is better adapted to model counts of all sources in the data space and hence a better separation of the background and sources terms.



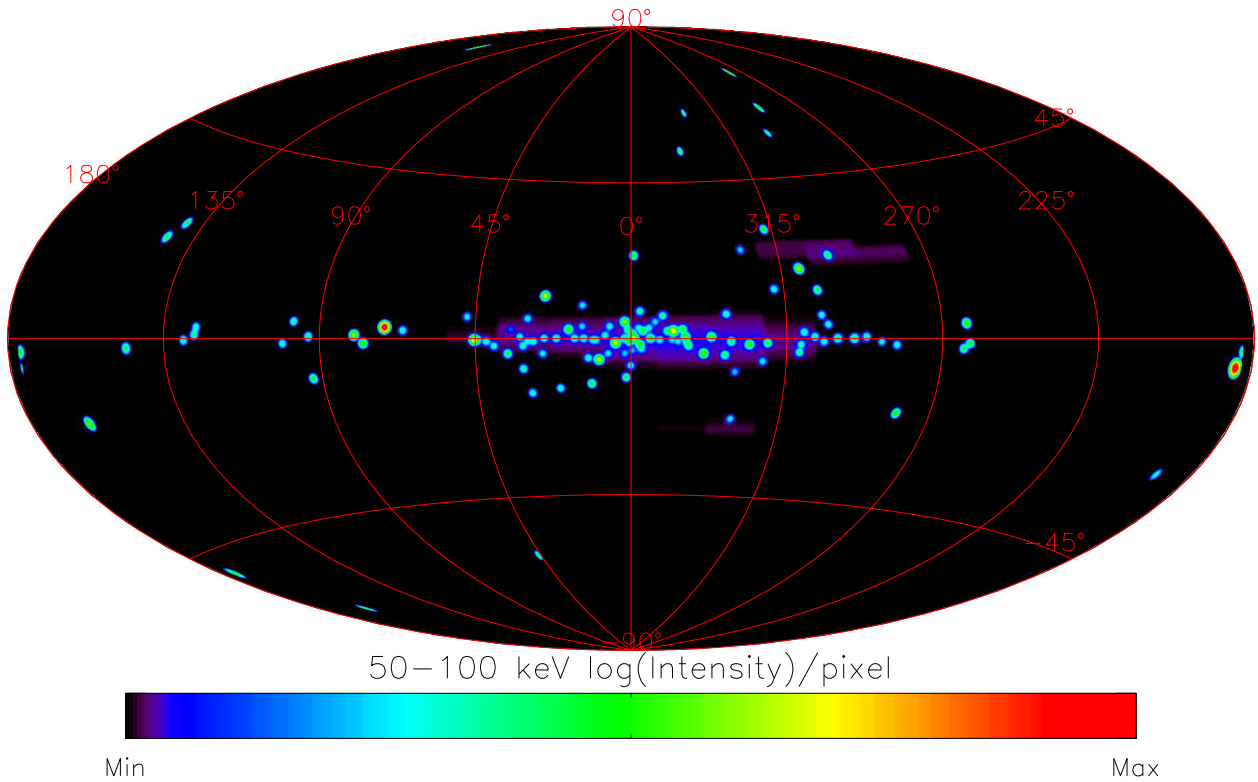


Fig. 2.— 50–100 keV intensity sky map including both sources and diffuse emission. The diffuse part of the image has pixels of different size and is first downsampled to a common pixel size of  $3^\circ \times 2.6^\circ$ , thereafter the image is smoothed by a  $3 \times 3$  pixels boxcar.

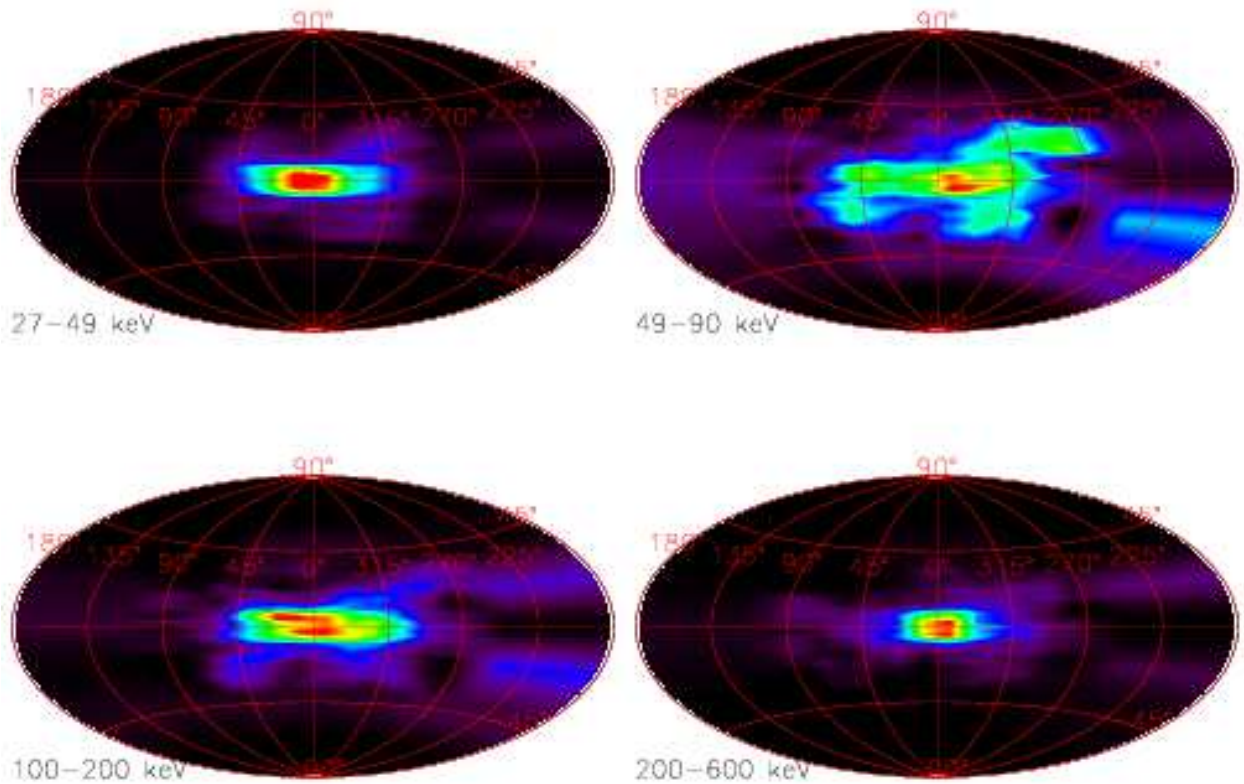


Fig. 3.— “Diffuse” emission intensity all sky maps. The energy bands are (top-left) 27–49 keV, (top-right) 49–90 keV, (bottom-left) 100–200 keV and (bottom-right) 200–600 keV. The original images have pixels of different size and are first downsampled to a common pixel size of  $3^\circ \times 2.6^\circ$ , thereafter they are smoothed by a  $3 \times 3$  pixels boxcar. The “Diffuse” emission energy is minimum in the 50–100 keV band. The color intensity is the same as in Fig. 2.

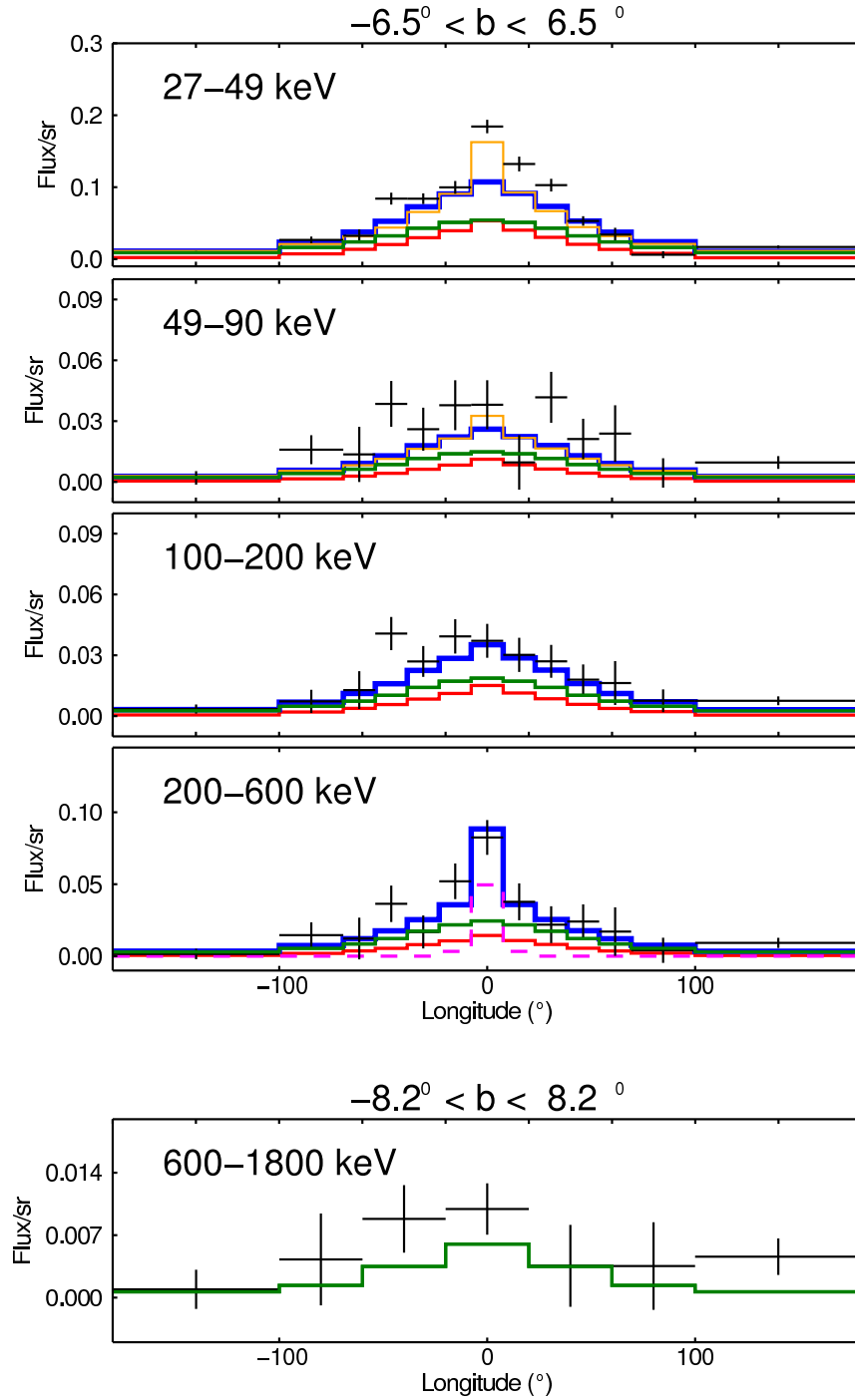


Fig. 4.— Longitude profiles of the Galactic Ridge emission in different energy bands, observed with *INTEGRAL/SPI* (crosses). The best fit template maps consisting of a combination of GALPROP IC distribution,  $A_{4.9\mu\text{m}}$ , and the annihilation radiation contribution (table 3) is shown in blue.  $A_{4.9\mu\text{m}}$  (stellar emission) and IC contributions are shown respectively in red and green. The pink dash-dotted line is the annihilation radiation contribution in the 200–600 keV energy band. The orange thin line (best absolute model) is a model consisting of IC plus DIRBE-based  $4.9\mu\text{m}$  template for energy below 49 keV and IC plus  $60\mu\text{m}$  emission map between 49 keV and 200 keV.

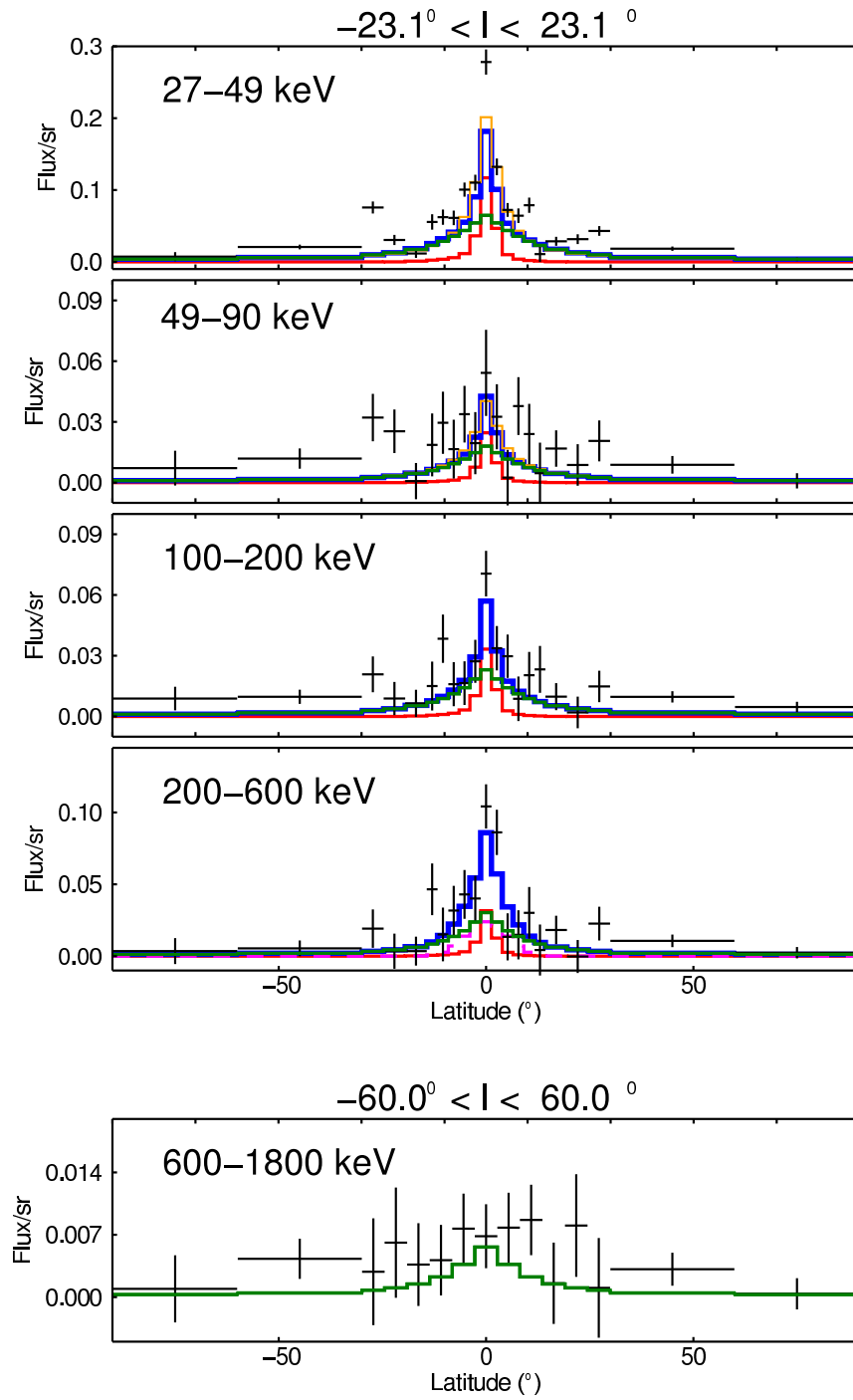


Fig. 5.— Same as Fig. 4, but for Galactic latitude.

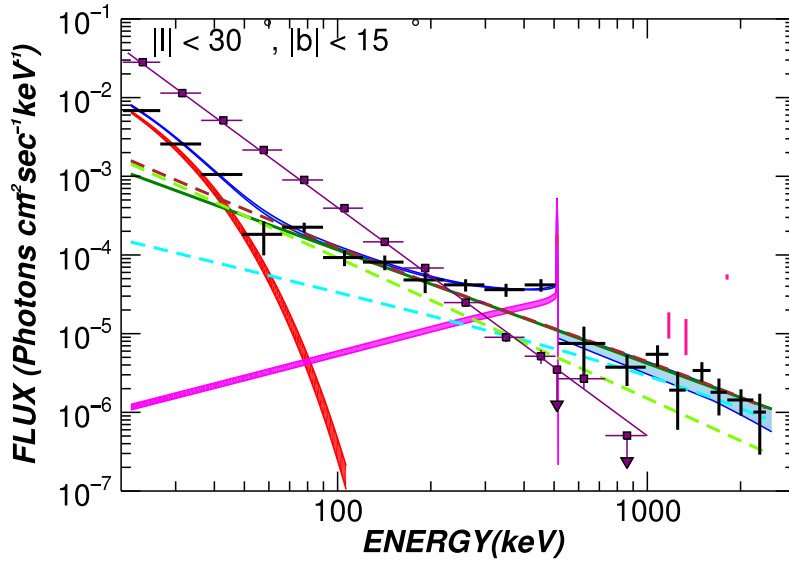


Fig. 6.— Spectra of the different emission components in the central radian of the Galaxy ( $|l| < 30^\circ$  and  $|b| < 15^\circ$ ). SPI measurements are black crosses. Violet squares: total emission of resolved sources. Violet line: power law fit to the resolved sources emission (power-law index of 2.9 and flux at 100 keV  $4 \times 10^{-4}$  ph cm $^{-2}$  s $^{-1}$  keV $^{-1}$ ). Blue: total diffuse emission – Magenta: annihilation radiation spectrum (line + positronium) – Red: Emission of low energy “unresolved” sources. The possible range of variation of these components are represented with the shaded area. Dark green line – is the deduced continuum emission thought to be dominated by CRs interacting in the ISM. The diffuse continuum best fit spectrum based both on spatial morphology and spectral decomposition is indicated by the dashed cyan ( $A_{4.9\mu\text{m}}$  spatial component) and green dashed lines (IC component). The sum of these two components is the brown dashed line which compared to the power-law fit with index 1.44 based solely on spectral decomposition (dark green line).

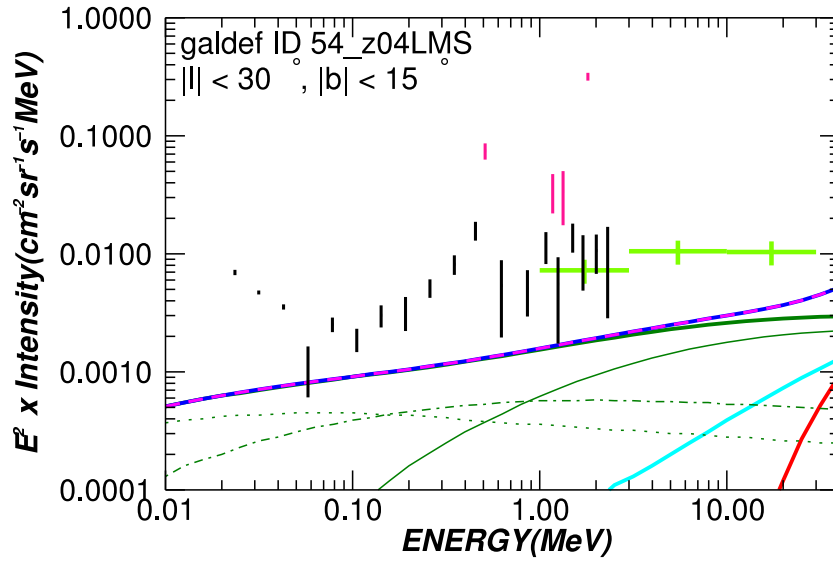


Fig. 7.— Spectrum of the diffuse emission for ( $|l| < 30^\circ$  and  $|b| < 15^\circ$ ). Black data points are for SPI (positron annihilation,  $^{26}\text{Al}$  and  $^{60}\text{Fe}$  lines are shown in red-pink). Green data points are for COMPTEL. The blue/pink line is the total emission as calculated with the GALPROP code, with the primary electron spectrum based on *Fermi-LAT* measurements. Green solid line: total Inverse-Compton emission (IC) – Red solid line :  $\pi^0$ -decay – green thin line : IC (optical) – Green short-dash thin line IC (IR) – Green dotted thin line: IC (CMB) – Cyan solid line : bremsstrahlung emission.

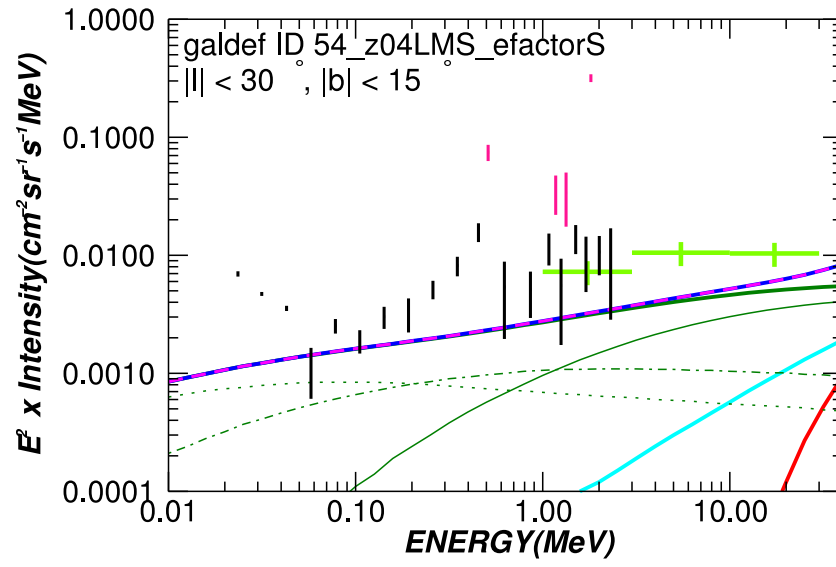


Fig. 8.— Same as Fig. 7, with the primary electron spectrum increased by a factor 2 relatively to that used in Fig. 7.

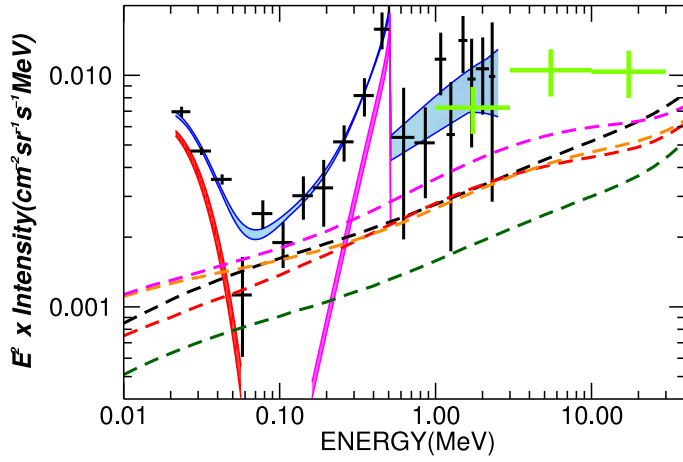


Fig. 9.— Same as Fig. 7 for different GALPROP configurations. The dashed lines are IC models: primary electron spectrum of Fig. 7 (dark green), primary electron spectrum increased by a factor 2 of Fig. 8 (black), increased halo height from 4 kpc to 10 kpc (red) and increased ISRF in the Galactic bulge ( $\times 10$ ) (orange) and both increased halo height from 4 kpc to 10 kpc and ISRF in the Galactic bulge ( $\times 10$ ) (magenta).

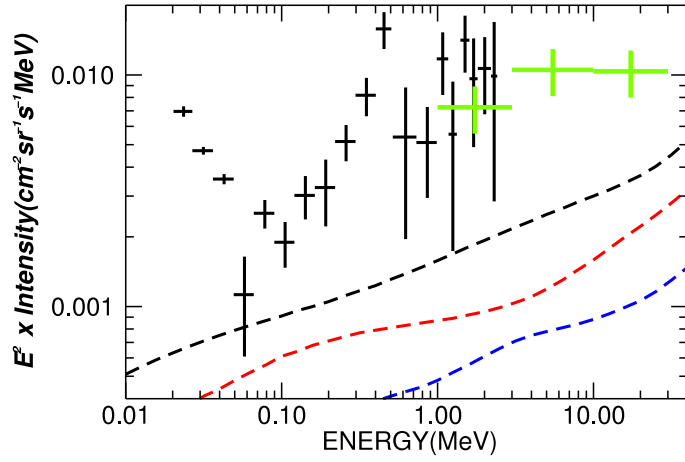


Fig. 10.— Data and model as in Fig. 7. The dashed dotted lines are IC models. Primary electron spectrum of Fig. 7 (black), same primary electron spectrum cutoff below 1 GeV (red), and same primary electron spectrum cutoff below 5 GeV (blue).

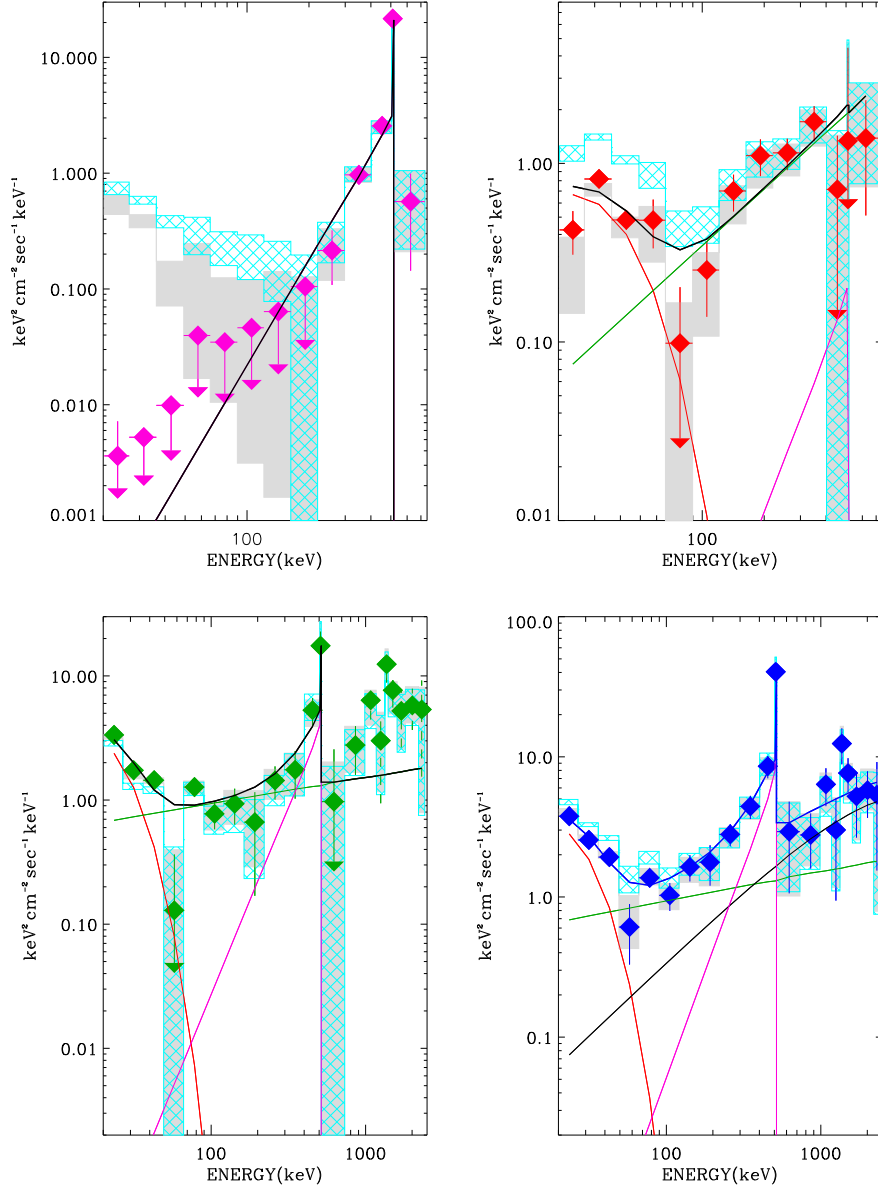


Fig. 11.— Spectrum of the diffuse emission for  $|l| < 30^\circ$  and  $|b| < 15^\circ$  for each extracted components. For each plot, the  $1\text{-}\sigma$  envelope obtained with the counts flux matrix, both for sources and diffuse, is shown as the cyan hatched region, while the spectrum that is obtained with the pseudo-efficiency for sources and counts flux matrix for the diffuse emission is shown as a grey-shaded region. The crosses and diamond symbols correspond to the components obtained with the pseudo-efficiency matrix for both sources and diffuse. The black line is the resulting emission spectrum. Upper left: magenta: annihilation radiation spectrum (line + positronium) Upper right: red: emission of “unresolved” sources, mainly cataclysmic variable and coronally active stars. Lower left: green line is the deduced interstellar emission. Lower right: the green line is the GALPROP IC power-law fitted on c), the red is the  $A_{4.9\mu\text{m}}$  power-law fitted on b), magenta is the deduced total annihilation radiation, blue points with the diamond symbol are the total diffuse emission while the blue continuous line is its best fitted model (sum of all diffuse fitted components).

Table 1. Information on exposures

Energy band (keV)	27–36	25–50	50–100	100–200	200–600	600–1800
Number of exposures	38699	38699	38699	38699	38699	36486
Reduced $\chi^2$	1.18	1.27	1.07	1.05	1.04	1.03
Degree of freedom	656914	649991	664354	666411	666595	628753
Number of point-sources	256	254	121	53	26	4
Number of parameters	15581	22504	8141	6084	5900	5606
Exposure maximum reduced $\chi^2(p)$	4.2	5.2	3.1	3.0	3.0	3.1
Exposures with						
Reduced $\chi^2(p) < 2$	38342	38690	38436	38471	38473	36450
Reduced $\chi^2(p) < 3$	38513	38232	38698	38698	38699	36485

Note. — Reduced  $\chi^2$  is the total chi-square between the data and the best sky model convolved with the instrument response divided by the degree of freedom. Reduced  $\chi^2(p)$  is the exposure chi-square divided by the number of working detectors (computed for each exposure p).

Table 2. Information on spectral energy bands

Energy band (keV)	20–27	27–36	36–49	49–66	66–90	90–121	121–163	163–220
Number of point sources	256	256	251	193	158	122	77	48
Reduced $\chi^2$	1.088400	1.178813	1.124047	1.058390	1.087771	1.031193	1.024928	1.025746
Degree of freedom	656914	656914	656921	664753	664804	666291	666370	666415
Energy band (keV)	220-298	298-402	402-505	505-516	516-732	732-988	988-1170	1170-1176
Number of point-sources	34	17	13	11	11	11	2	2
Reduced $\chi^2$	1.007953	1.006851	1.013379	0.999983	1.014998	1.002269	1.003606	1.000524
Degree of freedom	666587	666604	666608	666610	666610	628746	628755	628755
Energy band (keV)	1176-1330	1330-1336	1336-1400	1400-1600	1600-1806	1806-1812	1812-2200	2200-2414
Number of point-sources	2	2	2	2	2	1	1	1
Reduced $\chi^2$	1.000548	0.997189	0.999347	1.004202	1.003443	1.000153	1.002443	1.001612
Degree of freedom	628755	628755	628755	628755	628755	628756	628756	628756

Note. — PSD+PE data (38699 exposures) are used for energies below 650 keV and only PSD data (36486 exposures) above.

Table 3. Galactic diffuse morphology modelling with synthetic maps

Modelling with a single synthetic map							
Energy band (keV)	25–50	50–100	100–200	200–600	600–1200	1200–1800	600–1800
<i>1.25</i> $\mu$ m	345.1	84.5	119.7	74.4	<i>0.1</i>	<i>0.6</i>	<i>0.5</i>
2.2 $\mu$ m	181.9	65.7	85.6	47.0	3.0	1.3	4.5
3.5 $\mu$ m	153.7	55.0	76.6	45.3	5.4	1.6	7.4
4.9 $\mu$ m	160.3	46.8	75.0	55.8	7.7	1.8	10.1
12 $\mu$ m	961.6	90.4	109.6	78.8	8.6	4.3	12.6
25 $\mu$ m	1149.7	85.3	127.4	86.5	12.9	6.5	19.3
60 $\mu$ m	1000.0	54.7	82.8	73.6	14.4	5.8	20.4
100 $\mu$ m	850.9	50.7	76.0	68.1	11.5	4.9	16.2
140 $\mu$ m	863.1	56.1	86.9	74.2	10.6	5.0	15.2
240 $\mu$ m	952.9	74.9	111.6	88.1	10.4	5.2	15.3
<sup>a</sup> A <sub>2.2<math>\mu</math>m</sub>	574.2	75.4	101.3	50.7	5.5	2.3	7.1
<sup>a</sup> A <sub>3.5<math>\mu</math>m</sub>	483.6	51.5	69.8	37.8	6.0	2.9	8.0
<sup>a</sup> A <sub>4.9<math>\mu</math>m</sub>	447.8	29.1	71.0	45.8	7.6	4.9	11.3
<sup>a</sup> A <sub>12<math>\mu</math>m</sub>	647.0	31.0	82.7	54.5	9.6	6.3	14.6
CO	838.5	76.2	108.5	96.1	9.6	9.6	17.8
HI	1522.3	182.4	347.8	222.6	20.3	10.7	32.1
IC-ID54z04LMS	219.9	29.3	44.9	18.8	2.1	1.1	2.4
<b>IC-ID54z04LMS-efactor</b>	231.0	31.9	48.1	18.9	<b>2.1</b>	<b>1.1</b>	<b>2.4</b>
Degree of freedom	649992	664355	666412	666596	628747	628753	628753
Modelling with a combination of IC-ID54z04LMS-efactor (hereafter IC) plus another synthetic map							
Energy band (keV)	25–50	50–100	100–200	200–600	600–1200	1200–1800	600–1800
<i>IC + 1.25</i> $\mu$ m	180.8	31.9	47.8	18.9	<i>0.0</i>	<i>0.4</i>	<i>0.1</i>
IC + 2.2 $\mu$ m	59.0	30.2	33.1	17.3	1.5	0.7	1.6
IC + 3.5 $\mu$ m	23.8	25.6	25.7	14.3	2.0	0.7	2.1
<i>IC + 4.9</i> $\mu$ m	<i>9.1</i>	20.0	20.8	12.5	2.1	0.6	2.3
IC + 12 $\mu$ m	215.3	27.7	25.7	12.7	2.1	1.1	2.4
IC + 25 $\mu$ m	203.4	16.1	13.3	4.8	2.1	1.1	2.4
<i>IC + 60</i> $\mu$ m	196.2	<i>5.2</i>	<i>3.8</i>	<i>0.1</i>	2.1	1.1	2.4
IC + 100 $\mu$ m	188.8	9.9	10.9	5.6	2.1	1.1	2.4
IC + 140 $\mu$ m	193.7	13.2	17.0	9.0	2.1	1.1	2.4
IC + 240 $\mu$ m	215.4	21.7	27.2	13.0	2.1	1.1	2.4
IC + <sup>a</sup> A <sub>2.2<math>\mu</math>m</sub>	231.0	31.9	48.1	18.8	2.1	1.1	2.4
IC + <sup>a</sup> A <sub>3.5<math>\mu</math>m</sub>	221.7	29.7	39.9	15.3	2.1	1.1	2.4
<b>IC + <sup>a</sup>A<sub>4.9<math>\mu</math>m</sub></b>	<b>101.3</b>	<b>6.6</b>	<b>20.5</b>	<b>7.0</b>	2.1	1.1	2.4
IC + <sup>a</sup> A <sub>12<math>\mu</math>m</sub>	145.6	3.8	20.8	7.5	2.1	1.1	2.4
IC + CO	120.8	15.0	13.3	11.8	2.1	1.1	2.4
IC + HI	231.0	31.9	48.1	18.9	2.1	0.8	2.4
Degree of freedom	649991	664354	666411	666595	628746	628752	628752
Modelling with a combination IC plus all other (non IC) synthetic map							
Energy band (keV)	25–50	50–100	100–200	200–600	600–1200	1200–1800	600–1800
All maps*	0.0	0.0	0.0	0.0	0.0	0.0	0.0
Degree of freedom	649976	664339	666396	666580	628731	628737	628737

Note. — Results of template fitting in several energy ranges. Values of the maximum-likelihood ratio  $-2 \times (\ln L - \ln L_0) \approx \Delta\chi^2$ . The sky model consists of point sources + diffuse (maps) + bulge (Gaussian of  $3.2^\circ$  and  $11.8^\circ$  centered at  $l = -0.6^\circ$  and  $b = 0.0^\circ$  for energies below 516 keV, except for the “all map” case (\*) where the bulge is included for all energy bands. First column contains the synthetic map name used, first line displays the energy bands in keV unit. Note that the maximum-likelihood ratio is zero by definition for the “all maps” model (\*), which corresponds to the combination of the best models by band. (<sup>a</sup>) are IR extinction-corrected maps (Sec. 4.1). IC-ID54z04LMS and IC-ID54z04LMS-efactor are IC distribution maps computed with GALPROP code (Sec. 5.1). For each energy band, highlighted numbers and models are the absolute best fit model (bold-italic) and the model used throughout this analysis. The reduced  $\chi^2$ , for the model in bold, are 1.27, 1.07, 1.05, 1.04, 1.03, 1.01 and 1.02 respectively for the 25–50, 50–100, 100–200, 200–600, 600–1200, 1200–1800, and 600–1800 keV bands.

Table 4. Diffuse ( $|l| < 30^\circ, |b| < 15^\circ$ ) spectral fit

Spectral model	Parameter	Value
IC power law	index	1.79 (fixed)
	Flux ( $\times 10^{-4}$ ) at 100 keV	0.92 ph cm $^{-2}$ s $^{-1}$ keV $^{-1}$ (fixed)
A $_{4.9\mu\text{m}}$ power law plus cutoff	index	0.95 (fixed)
	Cutoff energy	3411 $^{+2371}_{-1170}$ keV
	Flux ( $\times 10^{-4}$ ) at 100 keV	0.34 ph cm $^{-2}$ s $^{-1}$ keV $^{-1}$ (fixed)
exponential cutoff	Cutoff energy	7.7 $\pm$ 0.1 $^{+0.7}_{-0.6}$ keV
	Flux ( $\times 10^{-4}$ ) at 50 keV	1.60 $\pm$ 0.06 $^{+0.40}_{-0.35}$ ph cm $^{-2}$ s $^{-1}$ keV $^{-1}$
Positronium continuum	Flux ( $\times 10^{-4}$ )	67.3 $\pm$ 14.6 $[\pm 22.4]$ ph cm $^{-2}$ s $^{-1}$
Gaussian line at 511 keV	Flux ( $\times 10^{-4}$ )	15.8 $\pm$ 2.7 $[\pm 4.1]$ ph cm $^{-2}$ s $^{-1}$
$\chi^2$ (dof)	23(16)	
<b>Fit of each of the extracted spatial component separately</b>		
<b>Bulge<sup>a</sup></b>		
Positronium contium	Flux ( $\times 10^{-4}$ )	28.9 $\pm$ 2.9 ph cm $^{-2}$ s $^{-1}$
Gaussian line at 511 keV	Flux ( $\times 10^{-4}$ )	9.1 $\pm$ 0.7 ph cm $^{-2}$ s $^{-1}$
$\chi^2$ (dof)	11(11)	
<b>Extracted A<math>_{4.9\mu\text{m}}</math> like spatial morphology component<sup>b</sup></b>		
Power law	index	0.95 $^{+0.02}_{-0.04}$ $^{+0.27}_{-0.33}$
	Flux ( $\times 10^{-4}$ ) at 100 keV	0.34 $^{+0.08}_{-0.04}$ $^{+0.21}_{-0.09}$ ph cm $^{-2}$ s $^{-1}$ keV $^{-1}$
Exponential cutoff	Cutoff energy	11 $\pm$ 1 $^{+6}_{-3}$ keV
	Flux at 50 keV	1.07 $^{+0.22}_{-0.25}$ $^{+0.62}_{-0.59}$ ph cm $^{-2}$ s $^{-1}$ keV $^{-1}$
Positronium continuum	Flux ( $\times 10^{-4}$ )	1.8 $^{+15.8}_{-1.8}$ ph cm $^{-2}$ s $^{-1}$ keV $^{-1}$
Gaussian line at 511 keV	Flux ( $\times 10^{-4}$ )	0.0 $^{+1.2}_{-0.0}$ ph cm $^{-2}$ s $^{-1}$ keV $^{-1}$
$\chi^2$ (dof)	11(13)	
<b>Extracted IC spatial morphology component<sup>c</sup></b>		
Power law	index	1.79 $^{+0.03}_{-0.04}$ $^{+0.25}_{-0.25}$
	Flux ( $\times 10^{-4}$ ) at 100 keV	0.92 $^{+0.17}_{-0.12}$ $^{+0.12}_{-0.17}$ ph cm $^{-2}$ s $^{-1}$ keV $^{-1}$
Eponential cutoff	Cutoff energy	6.3 $^{+0.5}_{-0.3}$ $^{+3.1}_{-2.1}$ keV
	Flux ( $\times 10^{-4}$ ) at 50 keV	0.61 $^{+0.28}_{-0.12}$ $^{+1.12}_{-0.51}$ ph cm $^{-2}$ s $^{-1}$ keV $^{-1}$
Positronium continuum	Flux ( $\times 10^{-4}$ )	35.7 $^{+21.0}_{-13.7}$ ph cm $^{-2}$ s $^{-1}$
Gaussian line at 511 keV	Flux ( $\times 10^{-4}$ )	6.8 $^{+4.1}_{-2.6}$ ph cm $^{-2}$ s $^{-1}$
$\chi^2$ (dof)	10(8)	

Note. — Spectral model fitting results using both spatial nmorphology and spectral decomposition information. For the overall fit (20 keV–2.4 MeV), channels containing  $^{26}\text{Al}$  and  $^{60}\text{Fe}$  lines are omitted, the annihilation line energy is fixed to 511 keV with a FWHM fixed to 2.5 keV. The separate component fitting results (a-c) applied to fix some parameters and to enable a multi-component fit rely on the data below 1 MeV. The quoted errors are for a single parameter of interest ( $\chi^2 = \chi^2_{\text{minimum}} + 1.0$ ) except for those indicated between parenthesis that are for a single spectral model and 2 free parameters simultaneously ( $\chi^2 = \chi^2_{\text{minimum}} + 2.35$ ).

Table 5. “Fermi bubbles”  $2\text{-}\sigma$  upper limits (Fluxes are in unit of  $10^{-3}$  ph cm $^{-2}$  s $^{-1}$  )

Energy band (keV)	25–50*	50–100	100–200	200–600	600–1800
Upper Galactic latitude bubble	< 1.6	< 1.8	< 1.3	< 1.5	< 1.2
Lower Galactic latitude bubble	< 1.6	< 1.8	< 1.3	< 1.5	< 1.2

Note. — \*For the 25-50 keV band (Sec. 7.1), the fluxes of all the sky components are constrained to be positive.